The Structural Disjoining Potential of Grain Boundary Premelting in Binary Alloys using Phase Field Crystal Model

by

Elizabeth Rowan

A thesis
presented to McMaster University
in fulfillment of the
thesis requirement for the degree of
Master of Applied Science
in
Materials Science and Engineering

Hamilton, Ontario, Canada, 2013

I hereby declare that I am the sole author of this thesis. This is a true copy of the thesis, including any required final revisions, as accepted by my examiners.

I understand that my thesis may be made electronically available to the public.

Abstract

A framework is described using the phase-field crystal model for the study of premelting in binary alloys through short-range interfacial interactions that arise from the structure of grain boundaries. A nonconserved model A formulation of PFC was used to model grain boundaries in two dimensions for several different angles of misorientation: 27.8^o, 21.8^o, 17.8^o, 13.2^o, 5^o. The character of the premelting transition, whereby a liquid-like film develops at a defect at temperatures below the melting point, changed with misorientation angle. An excess mass over the grain boundary can be defined as an analog to the liquid layer thickness due to premelting. It is found that low-angle grain boundaries remain at a relatively constant value of excess mass, and indeed can remain solid above the melting point. High-angle grain boundaries have a logarithmically increasing width that diverges at the melting point. A width-dependent energy can be defined called the disjoining potential that takes into account structure, interfacial and bulk energies to describe the liquid-layer width. The form of this disjoinging potential was found to be exponential and monotonically decreased as width increased for high angles and produced an attractive minimum for low angles. The results of this work were compared to a pure material from a previous study.

Acknowledgements

While writing this thesis I have become deeply grateful for the awesome people who I know, or who I have come to know in the last two years. I think in some way or another everyone in the ACSR (or Team Hoyt :D) helped me write this thesis, and they all certainly helped me develop as a researcher. You guys rock, and I want the connections we've made in these last two years to hold up forever. I'd like to especially thank Jonathan Stolle, Joel Berry and Nana Ofori-Opoku who all went above and beyond the call of duty.

Next I have to thank the people in my life who helped me keep going with this 'little' endeavour. You helped me get through the rough stuff with no second thoughts. You'll never know how much your contributions to this effort meant to me.

Finally to the big guys: Nik, thanks for making such an amazing atmosphere as the ACSR. I am so glad that you welcomed me in and gave me a home here.

Jeff: There is so many ways that you helped me out I can't even begin to count. It's safe to say that without you I couldn't have done this. I will always be grateful - and a part of Team Hoyt!

Thank you, everyone. Without you, I could not have done this.

Table of Contents

List of Figures

Chapter 1

Introduction

Set aside from the essentially mean field properties of the bulk phase, grain boundaries and their interactions are fundamentally important to processes such as crystallization. A phenomenon known as premelting exists whereby a stable, nanometer-scale, disordered, liquid-like film at the grain boundaries can exist at temperatures just below the melting point.

During the onset of premelting, a grain boundary will separate into two solid-liquid interfaces - this wetted configuration can greatly change the macroscopic properties of a polycrystalline material. By introducing a region of liquid internally, a metal's resistance to shear stresses will be greatly reduced. An example of a material failure caused by premelting is hot tearing, which causes a material to essentially rip open at the grain boundaries under the shear stresses experienced during rolling. As the melting point is approached from below the premelted liquid-like film will grow, until either diverging at the melting point, or overheating to remain solid in the liquid region for a short range of temperatures.

It is helpful to introduce a quantity known as the disjoining potential, $V(h)$, which allows a more quantitative description of the width of the liquid-like film, h. Considering only the bulk energies, in the solid region of the phase diagram the crystalline state will always be favoured. However, in a premelted system interfacial energies favour the formation of a liquid layer. The free energy cost of maintaining a solid grain boundary becomes less favoured than forming two solid-liquid interfaces, $\gamma_{GB} > 2\gamma_{SL}$, where γ is the excess free energy per unit area of the interface. Thus, the thermodynamics of premelting are governed by the balance between bulk and interfacial free energies:

$$\omega_{excess} = \triangle\omega h + 2\gamma_{SL} + V(h) \tag{1.1}$$

where γ_{SL} is the solid-liquid interfacial energy, $\omega_{excess} = (\omega_{total} - \omega_{localsolid})$ is the excess grand potential energy of the system due to the grain boundary and $\triangle\omega = (\omega_{bulkliquid} - \omega_{bulksolid})$ is the difference of bulk grand potential energies. Increasing grain boundary misorientation increases γ_{GB}, and thus it serves as a convenient parameter to vary in order to study a range of premelting behaviours.

The nanometer scale of the liquid-like films, high temperatures, and buried nature of grain boundary premelting make it difficult to observe and measure experimentally. There have been some attempts, such as imaging premelting in colloidal crystals using optical microscopy, (see figure 1) [1] as well as transmission electron microscopy and Auger spectroscopy for binary alloys [16][17] However, since atomistic-scale simulations can directly control grain geometry and external conditions by carefully choosing initial conditions, they are well-suited to capturing premelting behaviour.

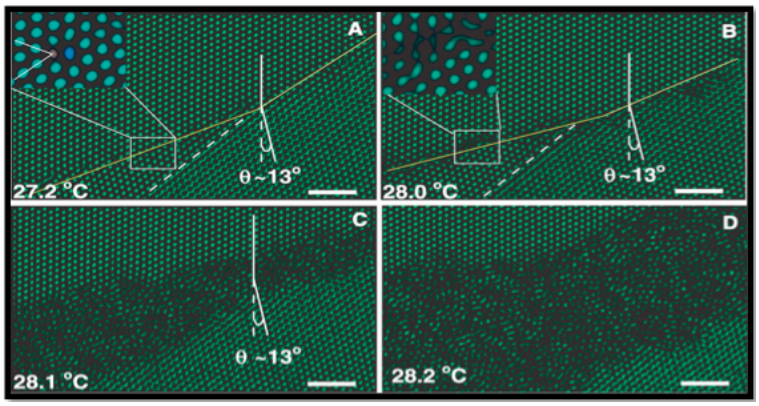

Figure 1.1: Work by A.M. Alsayed et al. Science 19 August 2005. Misorientated colloidal crystals show the effects of premelting.

Previous work has been done to study grain boundary premelting theoretically, for both pure materials and alloys using a variety of techniques. For pure materials, Monte Carlo simulations [3][4] and the lattice-gas model (in 2D) have confirmed grain boundary premelting, as well as giving a prediction for the form of the divergence of the liquid-like film width at the melting point. Molecular dynamics studies have found evidence of premelting behaviours that have a disjoining potential with a weakly attractive minimum that is not just based on misorientation. [11]. Multi-phase field models have studied premelting for alloys [23] [19]. It was observed that premelting could be induced by adding

solute to a dry grain boundary of a pure material. The addition of solute raises the dry grain boundary energy and allows the formation of a liquid-like film to become favourable. A premelting region was proposed to be added to the phase-diagram parallel to the solidus to account for the onset of premelting due to solute. Since the addition of solute raises the interfacial energy, It has been suggested that an alloy is likely to have larger widths at a given temperature then its pure counterpart. However, it is still unclear how the addition of solute effects the disjoining potential.

Grain boundary premelting will be studied here using the phase-field crystal model (PFC), which models polycrystalline materials as periodic structures in density. PFC has roots in the Swift-Hohenberg model, a model developed to study pattern formation and can be derived from classical density functional theory. The ability to simulate diffusive time scales and atomic length scales makes PFC a valuable tool for the study of the behaviour of grain boundaries.

Work was previously done by Mellenthin et al. [18] to determine the disjoining potential of a pure polycrystalline material using PFC, however there has been no exploration of the effect of solute addition to grain boundary premelting. Therefore, the goal of this work will be to study the structural disjoining potential of a premelted grain boundary in a binary alloy using PFC in order to elucidate the behaviour of the liquid film width as the system approaches the melting point.

Chapter 2

BACKGROUND - PREMELTING THEORY

2.1 Grain Boundary Structure

Observations of premelting in previous studies [5][15] have revealed key relationships between the structure of an interface and its characteristic film thickness. In order to elucidate these relationships grain boundary structure will be discussed first.

A grain boundary can form when coalescing crystal grains of different orientations impinge on each other, forming a region that is in general more disordered, less dense, and at a higher energy than the bulk crystal. Misorientation describes the angle of rotation of the orientation change between grains. If the axis of rotation can be defined in the same plane as the boundary then it is a tilt grain boundary [26]. This work deals exclusively with tilt grain boundaries. There are two types of tilt boundaries that will be considered based on the magnitude of the misorientation: low angle and high angle.

Low (or small) angle grain boundaries, shown in figure 2.1, are characterized by having a misorientation angle, θ, of less than approximately 15^o. For $\theta < 15^o$ some crystal planes will line up with the opposing plane in the neighbouring grain, matching one lattice point with another. However some lattice planes will not match up, and a dislocation will be formed. As the misorientation angle increases, more planes will not match up with the lattice in the neighbouring grain, causing the number of dislocations to increase and the spacing between dislocations to decrease.

High (or large) angle grain boundaries have $\theta > 15^o$, as seen in figure 2.1. At these

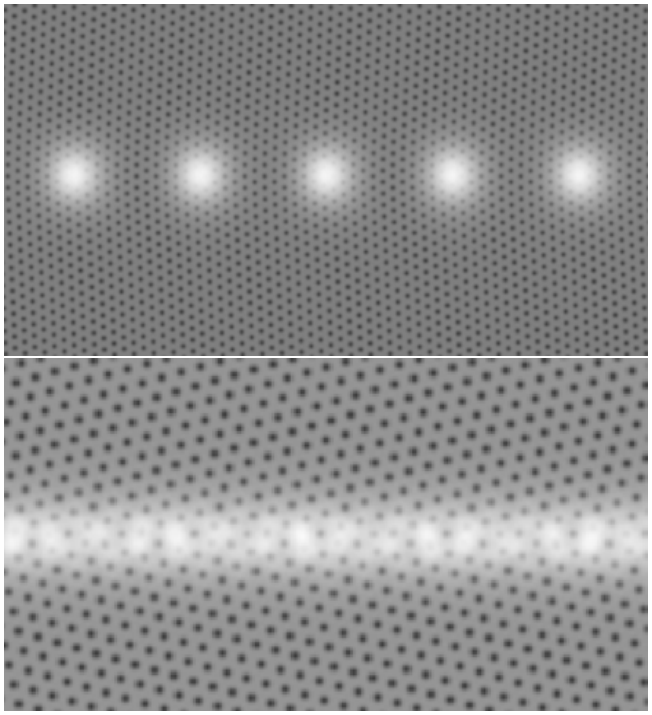

Figure 2.1: Top: A low angle grain boundary represented by a row of dislocations (white), Bottom:A high angle grain boundary represented by a disordered region (blurry white). Both are in a triangular lattice (atoms in black). Obtained using PFC simulation

angles, the dislocations have ceased being individually distinguishable, interacting in such a way as to distort the dislocation core from the core structure of an isolated dislocation in a crystal lattice. No long-range order exists for high angle boundaries, although some local ordering is possible.

Grain boundary interfacial energy, γ_{GB}, is structure dependent. Read and Shockley introduced a description of low-angle grain boundary energy in 1950 by considering the elastic contribution due to the localized stress field caused by a dislocation. For the low-angle regime, grain boundary energy increases as a function of misorientation:

$$\gamma_{GB} = E_0\theta(A - ln\theta) \tag{2.1}$$

$E_0 = \frac{Gb}{4\pi(1-\nu)}$ and $A = 1 + \ln(\frac{b}{2}\pi r_0)$, where G is the shear modulus, b is the Burgers vector, ν is poisson's ratio, and r_0 is the radius of the dislocation core.

In contrast, the grain boundary energy for high-angles changes very little with misorientation, as can be seen in figure 2.2. Equation 2.1 is not applicable for high angle grain boundaries. Once the dislocation cores begin to overlap, the elastic contribution can no longer describe the total energy and atomic interactions must be considered explicitly. [26]

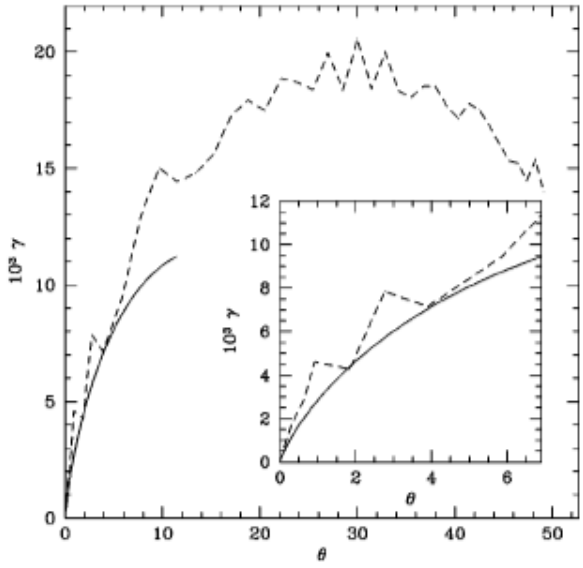

Figure 2.2: Grain boundary energy as a function of misorientation as determined by the PFC model (dashed line) and the Read-Shockley equation (solid line). [6]

At the interface, the lattice periodicity of the crystal is disrupted, causing excess energy from the broken interatomic bonds that would have been whole if there had been no interface. The more broken bonds there are per unit area, the higher the interfacial energy. [28] Therefore low angle grain boundaries can be expected to have a lower γ_{GB} than most high angle grain boundaries, which will in turn have less interfacial energy than a free surface. Exceptions exist, like twin boundaries which, while described by high angles of misorientation, can have very low γ_{GB}.

In alloys, solute preferentially segregates to interfaces. The disordered region of a grain boundary provides a large number of sites for solute atoms to attach. High angle grain boundaries accumulate solute within a distance of one or two atomic spaces from the boundary midplane. This suggests that the overlapping dislocation cores were attracting solute more strongly than other areas in the lattice. [26] While the degree of segregation will depend on the specific grain boundary structure, in general high angle boundaries will segregate more solute than low angle boundaries. If increasing misorientation increases

dislocation core density, then that suggests that increased misorientation also increases the amount of solute segregation.

2.2 Solid-Liquid Transitions

The familiar phenomenon of melting is well known to progress through the mechanism of nucleation. Fluctuations in various thermodynamic parameters occur frequently in a material. However, when the solid is heated to past the melting temperature, $T > T_m$, the liquid free energy becomes less than the solid free energy. This change in preferred phase from solid to liquid allows the potential for lasting small nuclei of liquid phase to form and grow. If the free energy benefit of creating the liquid phase can balance or outweigh the energy cost of forming a solid-liquid interface then the nuclei will be stable. If the volume of the nuclei is not enough to 'pay' the interfacial solid-liquid energy cost, the nuclei will disappear back into its parent solid phase. Heterogeneous nucleation occurs when a nucleus forms on a defect - be that an impurity, surface, grain boundary or any other site that will lower the energy cost of the solid-liquid interface. [13]

At temperatures below the melting point, there exists another mechanism for melting other than the bulk melting predicted by the phase diagram - premelting. Regions of partial order, analogous to a liquid, appear due to the benefit of forming solid-liquid interfaces. These stable, nanometer width films form heterogeneously at defects. As T_m is approached from below, the film grows until eventually complete melting is attained at or past the melting point. Of particular interest is the influence of these 'premelted' films on macroscopic quantities due to the difference in properties between the film and a bulk system, as seen in hot tearing. (Described in section 1) [2] [16]

2.3 Premelting Thermodynamics

The effects of premelting have been observed in a diverse selection of materials in such number that it could be suggested that this phenomenon is characteristic of any material in the solid phase. The basic process requires only that the interfacial structure causes the relative surface energies between solid-solid and solid-liquid to shift, such that the formation of two solid-liquid interfaces are favoured. [27]

A premelted grain boundary, as shown in figure 2.3, replaces the once dry solid-solid interface with two solid-liquid interfaces. The distance between the solid-liquid interfaces

Figure 2.3: A premelted grain boundary, where h is the film width

is known as the film width or thickness and is denoted as h. The film width for a typical high-angle grain boundary under premelting conditions will increase continuously with temperature until diverging at the melting point, as seen in figure 2.4 curve a). This behaviour can be described through complete wetting (figure 2.5).

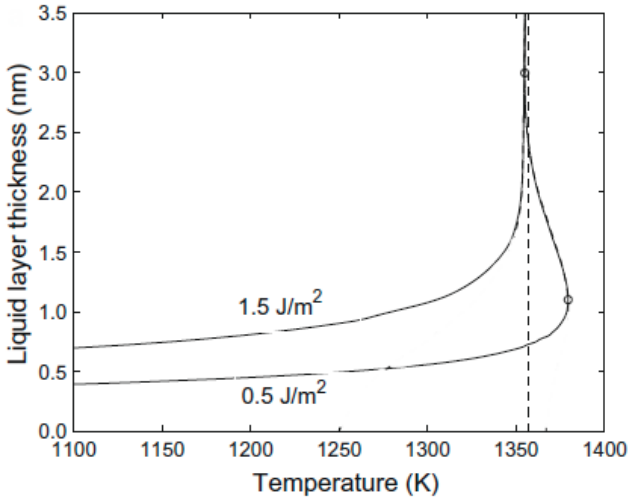

Figure 2.4: Characterization of film thickness with temperature for different grain boundary energies, γ_{GB}. The vertical dashed line indicates the melting temperature. Simulated using multi-phase field model. Modified from [19]

Wetting describes the interaction of a liquid and a solid substrate. A drop of liquid will conform to a shape determined by the relative surface energies between the liquid, the solid, and the surrounding medium – usually air. In this way, premelting can be described in the language of wetting, where instead of two different materials as the liquid and solid, it is the solid and its own melt.

Young's equation is a well-known expression that relates the contact angle, to the

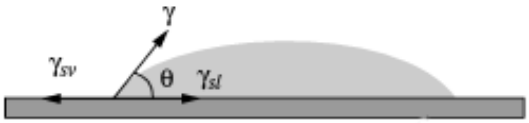

Figure 2.5: A liquid drop on a solid substrate. [25]

interfacial energies of a free surface.

$$\cos\theta = \frac{(\gamma_{SV} - \gamma_{SL})}{\gamma} \tag{2.2}$$

Where γ_{SV}, γ_{SL}, and γ, are the interfacial energies between at the solid-vapour, solid-liquid, and liquid-vapour respectively. θ is the contact angle. The contact angle is the angle between the liquid surface and substrate, as measured through the liquid. For a premelted grain boundary, Young's equation can be adapted to:

$$\cos\theta = \frac{(\gamma_{GB} - \gamma_{SL})}{\gamma_{SL}} \tag{2.3}$$

Where γ_{GB} is the excess energy due to the grain boundary of a completely 'dry' system (i.e. one without a premelted film). Under complete wetting conditions the contact angle goes to zero, giving a relation of:

$$\begin{aligned} 1 &= \frac{(\gamma_{GB} - \gamma_{SL})}{\gamma_{SL}} \\ 0 &= \gamma_{GB} - 2\gamma_{SL} \end{aligned} \tag{2.4}$$

If $\gamma_{GB} = 2\gamma_{SL}$ then it is just as favorable for a system to choose to maintain two solid-liquid interfaces as opposed to one solid-solid interface - i.e. the grain boundary. This idea can be extended into a premelting criterion:

If $\gamma_{GB} > 2\gamma_{SL}$, then the system will premelt.

Conversely, if $\gamma_{GB} < 2\gamma_{SL}$, then the system will not premelt.

It becomes clear that with only the information presented on an equilibrium phase diagram a 'premelting region' cannot be identified. The crystalline state will always be

favored in the solid region. The creation of a disordered liquid-like film is an interface driven phenomenon, reliant on more than the bulk energies. However the premelting criterion is a necessary but not sufficient condition for a film width to be measurable, as will be discussed in section 2.4.

Any factor that increases γ_{GB} can cause $\gamma_{GB} > 2\gamma_{SL}$ to be satisfied and premelting to be induced. For grain boundaries, misorientation is a convenient choice of parameter to vary in order to study the effect of the change of γ_{GB} on premelting. High angle grain boundaries are more likely to induce premelting due to a higher γ_{GB} (figure 2.2). The converse is true for low angle grain boundaries. For this thesis, misorientation shall be focused on for the study of premelting and γ_{SL} will be taken as a material constant.

2.4 Structural Disjoining Potential

While the premelting criterion is a necessary condition to determine if a system will premelt, it cannot provide information about the premelted film width. $\gamma_{GB} > 2\gamma_{SL}$ also gives no information about competition between the bulk and interfacial energies. The criterion does not take into account the energy cost of the formation of a (unfavored) liquid-like region from the (favoured) solid, reducing the volume of the solid phase. In order for a liquid-like film to form:

$$\gamma_{GB} > 2\gamma_{SL} + \Delta f_{Bulk} h + V(h) \tag{2.5}$$

where $\Delta f_{Bulk} = f_{liquid} - f_{solid}$. The second term represents the inherent energy cost for inserting a width, h of the unfavoured liquid phase into the system, where a unit cross-sectional area has been assumed. In addition to the bulk and interfacial contributions to this new sufficient condition there is also a structural contribution, $V(h)$, from the interaction of the solid-liquid interfaces through the film. $V(h)$ is known as the structural disjoining potential. The exact form of $V(h)$ is not well understood.

By framing the premelting phenomenon in terms of a disjoining potential, the behaviour of the premelted film width can be explored. Equation 2.5 can be restated to solve for a value for the disjoining potential:

$$V(h) = \gamma_{GB} - 2\gamma_{SL} - \Delta f_{Bulk} h \tag{2.6}$$

Below the melting point, if $\gamma_{GB} > 2\gamma_{SL}$ then $V(h)$ will be positive. This result is typically found in grain boundaries whose liquid film width increases monotonically before

diverging at the melting point, i.e. complete wetting (see figure 2.4, curve a.). This behaviour is thought to arise from short-ranged structural interactions between the solid-liquid interfaces. [11]

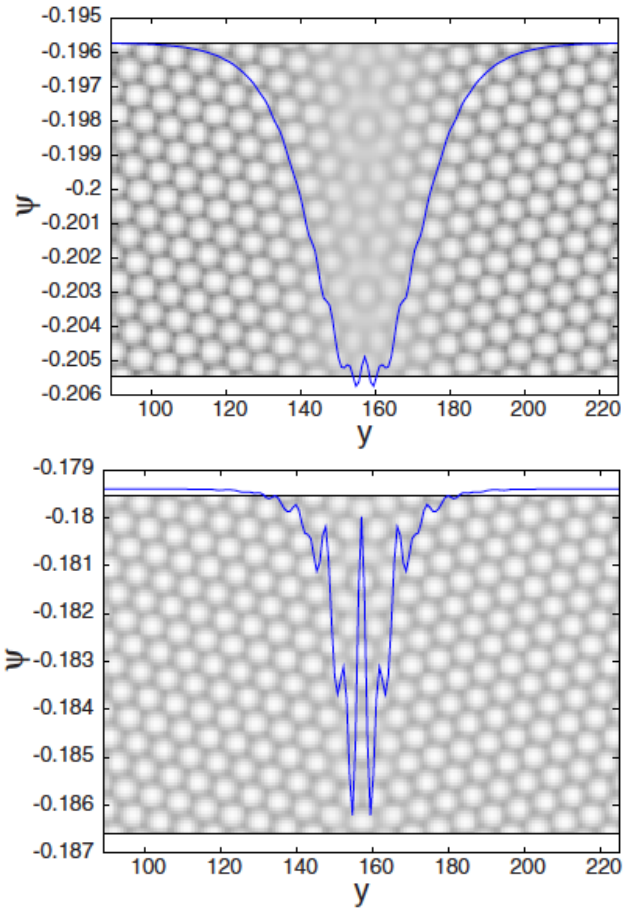

Figure 2.6: Shows the overlap of the density profile, indicating a diffuse interface. From these pictures can see that a liquid-like film doesn't approach the bulk liquid properties until at high h. (Top: closer to the melting point, Bottom: further from the melting point)

If, instead, $V(h) < 0$, then an attractive interaction between interfaces will occur, and the grain boundary will typically remain dry to the melting point. There exists another type of interface interaction where both long-range attractive and short-range repulsive forces cause a disjoining potential that has both an attractive and repulsive component. This attractive-repulsive interaction leads to a grain boundary that maintains a finite width

as the melting point is approached, and must be overheated (i.e. $T > T_m$) in order to fully melt the system. Figure 2.4 b. demonstrates this behaviour.

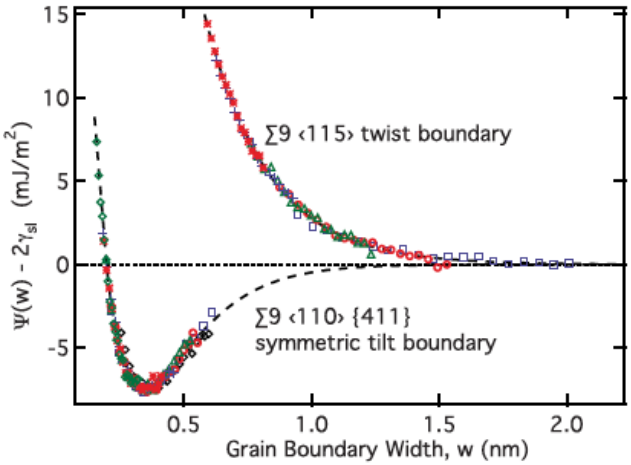

Figure 2.7: Disjoining potential as predicted in an MD simulation. A twist grain boundary is found to be repulsive, and a tilt boundary is found to be attractive-repulsive. [11]

The attractive-repulsive disjoining potential is characterized by having a weak attractive minimum in the disjoining potential. In figure 2.7, it can be seen that the grain boundary starts out as repulsive at small widths, causing a liquid film to appear. At higher widths, attraction becomes dominant and the liquid film is kept from diverging by the dispersion forces. This interesting case is difficult to predict, because it appears to have a complex dependence on width, and by extension, the structure of the grain boundary.

A form for $V(h)$ has been suggested from mean-field arguments and lattice-gas models for the diverging width of a high energy, repulsive grain boundary:

$$V_{rep}(h) = 2\gamma_{SL} + \Delta\gamma \exp(\frac{-h}{\delta}) \tag{2.7}$$

Where $\Delta\gamma = \gamma_{GB} - 2\gamma_{SL}$ and δ is an interaction length on the order of the atomic spacing. Similarly, a form has been proposed for a disjoining potential with an attractive minimum,

$$V_{att}(h) = 2\gamma_{SL} + \Delta\gamma_1 \exp(\frac{-h}{\delta_1}) + \Delta\gamma_2 \exp(\frac{-h}{\delta_2}) \tag{2.8}$$

Chapter 3

BACKGROUND - MODEL THEORY

Connecting length scales is of great interest in microstructure modelling; equally interesting is the consideration of long time scales. Due to a computationally efficient formulation, the Phase-Field Crystal model (PFC) can simulate both diffusive timescales and atomic length scales, which allows for the study of microscale structures like grain boundaries and dendrites. In the next section the PFC Free Energy functional for a pure material will be introduced.

3.1 The PFC Free Energy Functional

The basic PFC free energy functional for a pure material is:

$$F_{PFC}[n(\mathbf{r})] = \int d^3\mathbf{r}[\frac{n}{2}[\epsilon + (1+\nabla^2)^2]n + \frac{n^4}{4}] \tag{3.1}$$

Where $n(r)$ is the dimensionless number density, and is itself a function of $\mathbf{r}$, the radial spatial component, ϵ is a control parameter that is related to the temperature difference from the melting point. This free energy can be minimized, $\frac{\delta F_{PFC}[n(r)]}{\delta n(r)} = 0$ by periodic solutions. The density field is sinusoidal in the solid, but goes to a constant value in the liquid region. An interface width, as seen in figure 3.1, can be defined, ξ that is on the scale of nanometers. The amplitude of the periodic density structure is a convenient order

parameter that can be defined as varying between zero in the liquid and non-zero in the solid.

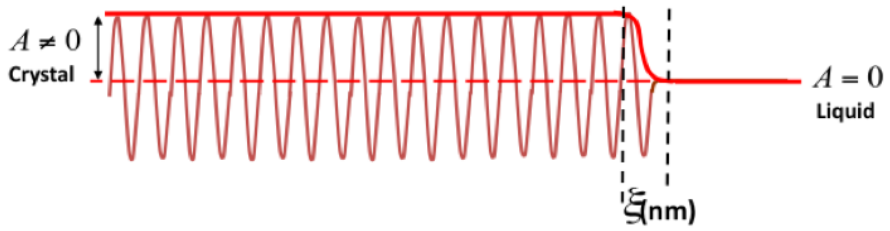

Figure 3.1: A profile of a solid crystal meeting a liquid region at an interface of width ξ. Adapted from [21] by Michael Greenwood.

The peaks of the sinusoidal wave can roughly be described by the general location of an atom on a lattice site. In a 2D simulation, a peak in the density field looks like a bright point. Notice in figure 3.2 how the grain boundary (line through the middle of the picture) is slightly diminished in brightness. This change in appearance is because the interface is at decreasing amplitude compared to the bulk solid region due to disorder.

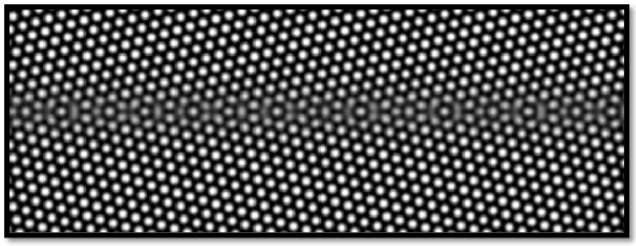

Figure 3.2: A 2D periodic structure in the density field is visible by the bright peaks in a constant configuration. A grain boundary occupies the middle of the frame.

3.2 Derivation from Classical Density Functional Theory (CDFT)

Classical density functional theory was developed to consider the coarse-grained properties of various physical systems. In the mid-1970's [22], it was developed further to explore liquid-solid phase transitions and has since become well known for its success with solving

first-order phase transitions in general. In this theory, the continuum atomic density field, $\rho(r)$, is averaged either in time or over the ensemble, and varies in amplitude between the solid and liquid phases. $\rho(r)$ is not the same as the dimensionless number density $n(\mathbf{r})$, which will be detailed later. The solid phase is represented by highly localized peaks in $\rho(r)$ that represent the probable locations of atoms in the lattice. $\rho(r)$ goes to a constant value while in the liquid. [2] From this continuous density field description of a solid-liquid system in CDFT, the phase-field crystal (PFC) model can be derived by simplifying it. This treatment of the PFC derivation will follow closely with methods used in [2], and [21] The CDFT free energy functional can be understood as containing three distinct contributions. The functional is written as:

$$F(\rho(r)) = \int [f_{ideal} + f_{interaction} + f_{external}]dr \tag{3.2}$$

where, $f_{ideal} = \rho(r)\ln(\frac{\rho(r)}{\rho_l}) - \delta\rho(r)$ is the non-interacting ideal gas free energy, ρ_l is a reference average number density and $\delta\rho(r) \equiv \rho(r) - \rho_l$. It should also be noted that f_{ideal} is just the free energy due to the atoms themselves being present. It is related to the entropy of the system - what configurations the atoms in the system can take. [2] This term drives the system toward a uniform field, which describes the liquid phase. $f_{interaction}$ is the excess free energy contribution due to many-body interactions in the system. Crystals can be classically described as a series of multi-body interactions to a first order approximation. [10] The contribution from $f_{interaction}$ to the total free energy will drive the system towards a periodic state, which describes the solid phase, when sufficiently large. $f_{external}$ is the additional free energy due to an external potential, such as a magnetic field. In the discussion to follow, the contribution to the total free energy from external sources will be assumed equal to zero.

The CDFT free energy functional can additionally be described through a Taylor series of correlation functions, as described in the Yussoff and Ramkrishnan model. [22] Correlation functions describe the interatomic interactions between a given number of 'bodies'.

$C_2(|r_1 - r_2|) = C_2(\mathbf{r})$

is the two-point correlation function and describes two-body interactions, C_3 is the three-point correlation function describes three body interactions, etc. [2]

The Helmholtz free energy can be expanded in relation to a liquid reference energy at coexistance, F_l, such that $\Delta F \equiv F - F_l$. It can also be scaled by k_BT where k_B is Boltzmann's constant and T is the temperature, to give:

$$\Delta F = \int dr[C_1(r_1)\delta\rho(r_1)+\frac{1}{2!}C_2(r_1,r_2)\delta\rho(r_1)\delta\rho(r_2)+\frac{1}{3!}C_3(r_1,r_2,r_3)\delta\rho(r_1)\delta\rho(r_2)\delta\rho(r_3)+\cdots] \tag{3.3}$$

Ramakrishnan and Yussouff [22] provided a link between the first term in equation 3.3 and f_{ideal}. Thus the remaining terms correspond with $f_{interaction}$ for CDFT. For PFC, $f_{interaction}$ can be simplified to only contain the two-body interactions and thus equation 3.3 is truncated at the two point correlation function. To proceed with the derivation of PFC from this more fundamental formalism, two key steps must be taken. First, it is useful to define a dimensionless number density in terms of ρ and with respect to ρ_l:

$$n \equiv \frac{\rho(r)-\rho_l}{\rho_l} = \frac{\rho(r)}{\rho_l} - 1 \tag{3.4}$$

Introducing this new parameter to f_{ideal} yields:

$$f_{ideal} = \rho_l(n+1)\ln(n+1) - (\rho_l(n+1)-\rho_l) \tag{3.5}$$
$$= \rho_l[(n+1)\ln(n+1) - (n+1-1)] \tag{3.6}$$
$$= \rho_l[(n+1)\ln(n+1) - n] \tag{3.7}$$

A taylor expansion of the term $(n+1)\ln(n+1)$ yields:

$$n + \frac{n^2}{2} - \frac{n^3}{6} + \frac{n^4}{12} - \frac{n^5}{20} + \cdots \tag{3.8}$$

Substitution of this expansion into the ideal energy term and keeping terms up to fourth order, we have:

$$f_{ideal} = [\frac{n^2}{2} - \frac{n^3}{6} + \frac{n^4}{12}]\rho_l \tag{3.9}$$

With the second step $C_2(|r_1 - r_2|)$ is expanded in Fourier space as k^2 around $k = 0$ up to k^4. This step assumes that the full two-point correlation function can be well described by:

$$C_2(k) = -c_0 + c_2k^2 - c_4k^4 \tag{3.10}$$

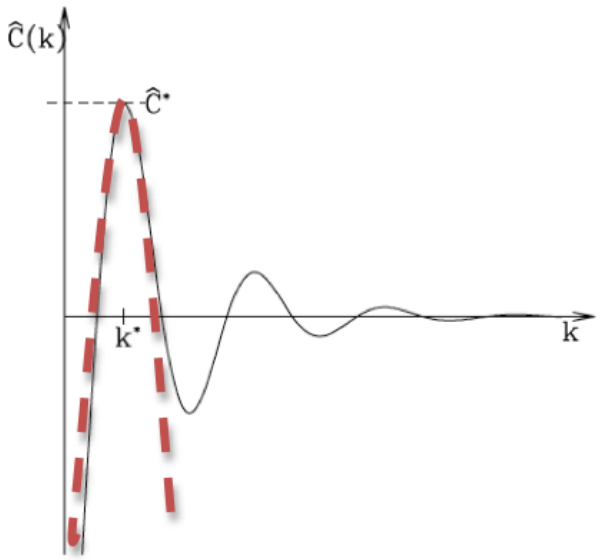

Figure 3.3: A representation of the two-point correlation function in Fourier space. [21] The red dashed line represents a fit to $C_2(k)$ used in the standard PFC approach. Any k values for which $C_2(k) > 0$ will be preferred by the system. Thus, structures with characteristic lengths corresponding to k values with large peaks will be formed in the system.

Where c_0, c_2 and c_4 are constants that can be fit to the first peak of $C_2(k)$ in figure 3.3.

Taking the inverse Fourier transform of equation 3.10 yields two laplacian terms which when combined with equation 3.9 result in the PFC free energy functional:

$$\Delta F = \int dr[\frac{n^2}{2} - \frac{n^3}{6} + \frac{n^4}{12}] + [-c_0 n^2 + n(c_2\nabla^2 + c_4\nabla^4)n] \tag{3.11}$$

where ρ_l can be absorbed into the scaling of ΔF. A series of coefficients can be introduced such that the PFC free energy functional takes on easily adjustable parameters to various physical material features [21]:

$$\Delta F = \int dr[\frac{B_l}{2}n^2 - t\frac{n^3}{3} + v\frac{n^4}{4}] + [\frac{B_x}{2}n(2R^2\nabla^2 + R^4\nabla^4)n] \tag{3.12}$$

where

$$t = \frac{1}{2}, v = \frac{1}{3}, B_l \equiv 1 + \rho c_0, B_x \equiv \frac{\rho c_2^2}{4c_4}, R \equiv \sqrt{\frac{2|c_4|}{c_2}} \tag{3.13}$$

B_l is the isothermal compressibility in the liquid phase, and B_x is the compressibility in the solid phase. R is the spacing of atoms, and $\Delta B_0 = B_l - B_x$ is a temperature scale.

3.3 Properties of PFC

3.3.1 Triangular Lattice

To find what kind of lattice structures minimize the free energy it is possible to do a one-mode approximation of the density field and minimize with respect to several intensive parameters, like T, average n, etc. For free energy functionals similar to equation 3.1 (like the Swift-Hohenberg model, Landau-Brazovskii model, etc. [2]), the structures that minimize it are already known [9]. A triangular phase is one of the simplest structures to minimize the PFC free energy functional in 2D. In order to construct a phase diagram for the triangular phase, the free energy must be minimized based on the one mode approximation and several non-constrained variables like wave number and amplitude. By minimizing the free energy with respect to non-constrained variables they are effectively minimized out so that a minimization based only on a constraint quantity can be reached. The two variables that will be left will be temperature and average density, and with these two quantities, a phase diagram can be built.

3.3.2 Rotational Invariance

In order for misorientation to occur in simulation, isotropy must be preserved in the continuum fields that govern the system. Isotropy requires that no one direction is favoured over any other direction. To successfully maintain misorientation between separate crystal grains all misorientations must be equally favourable. If the system had long-range order only in specific directions, the free energy of one orientation would be preferential to another and the system would shift to that lower free energy. Since the PFC free energy is invariant under rotation, multiple crystal orientations can exist simultaneously because they all have equivalent energy.

3.3.3 Elasticity

The exact form of the periodic solutions that minimize the free energy determines the crystal lattice structure that is produced. One of the simplest periodic solutions to the PFC free energy functional produces a triangular lattice in 2D. Minimizing the free energy functional in this way naturally captures elasticity. Consider a sinusoidal density field describing a solid, such as in figure 3.4.

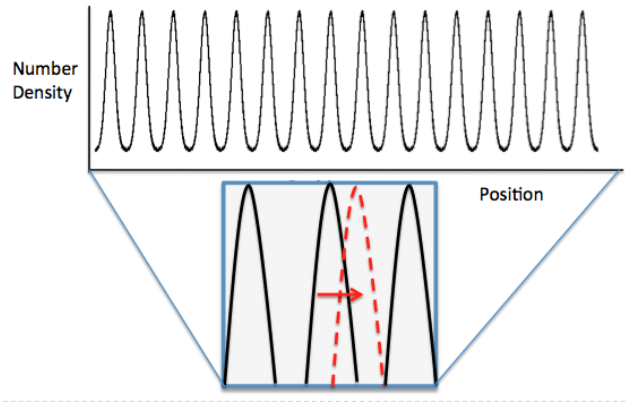

Figure 3.4: If a peak in the number density is shifted, the system can elastically relax the peak back to its original position to lower the free energy back to a minimum value.

Since the lowest energy state is described by a periodic density field, then there is some wavelength that the system prefers. If a density peak is shifted in such a way that it is no longer at this preferred wavelength, the system will be at a higher free energy then its minimum free energy. In order to return to this lowest energy the system must return the shifted peak to the location described by the preferred wavelength. This natural relaxation back to a given starting position suggests elastic properties in the system. Consider a system governed by a characteristic length scale, a, like a preferred wavelength. Its free energy can be described by an expansion of a around its equilibrium value; this is analogous to shifting the density peak from its equilibrium position.

$$f(a) = f(a_{eq}) + \frac{\delta f(a)}{\delta a}|_{eq}(a - a_{eq}) + \frac{1}{2}\frac{\delta^2 f(a)}{\delta a^2}|_{eq}(a - a_{eq})^2 + \cdots \tag{3.14}$$

The characteristic length scale must be able to minimize the free energy, thus $\frac{\delta f(a)}{\delta a}|_{eq} = 0$, and the expansion at second order becomes:

$$f(a) - f(a_{eq}) = \frac{1}{2}\frac{\delta^2 f(a)}{\delta a^2}|_{eq}(a - a_{eq})^2 + \cdots$$

where the spring constant can be defined as $k \equiv \frac{\delta^2 f(a)}{\delta a^2}$. This brings the above equation in line with Hooke's Law:

$$\Delta f = \frac{1}{2}k(\Delta a)^2 \tag{3.15}$$

3.4 Simulating Binary Alloys using PFC

The Phase Field Crystal model can be extended to study binary alloys, by using two continuum fields - dimensionless number density and dimensionless concentration. Similar to the discussion for the pure material, a derivation of binary PFC can be done from CDFT by including the free energy functionals of each of the species as well as a two component mixing term. The first proposal of a binary PFC was introduced by Elder et al. [9]

The same steps used for the pure material can be followed for the binary case. [2] The total free energy functional can be described as:

$$F = \int dr[f_{AA} + f_{BB} + f_{AB}] \tag{3.16}$$

By incorporating the separate contributions to the free energy from each species, A and B:

$$F = \int dr([f^A_{ideal}A + f^A_{interaction}A] + [f^B_{ideal}B + f^B_{interaction}B] + [f^A_{interaction}B]) \tag{3.17}$$

After expanding $C_2(|r_1 - r_2|)$ in Fourier space as k^2 around $k = 0$ up to k^4, and introducing the dimensionless number density, n, both f_{AA} and f_{BB} goes to:

$$f_{AAorBB} = \frac{n_{AAorBB}}{2}[r + (1 + \nabla^2)^2]n_{AAorBB} + \frac{n^4_{AAorBB}}{4} \tag{3.18}$$

While f_{AB} goes to:

$$f_{AB} = n_{AB}[r + (1 + \nabla^2)^2]n_{AB} \tag{3.19}$$

Again, $r \sim T - T_c$ as introduced as in section 3.1

Finally, a species concentration field can be introduced [2]:

$\psi = \frac{n_A}{(n_A+n_B)}$

where $n = n_A + n_B$. This allows the definition of a final binary free energy functional [7]:

$$F_{PFC} = \int (\frac{n}{2}(\Delta B_0 + B_2^l\psi^2 + B_0^x(1+\nabla^2)^2)n - \frac{t}{3}n^3 + \frac{v}{4}n^4 + \frac{w}{2}\psi^2 + \frac{u}{4}\psi^4 + \frac{K}{2}|\Delta\psi|^2)d\vec{x} \tag{3.20}$$

Where B_2^l, K, w, u and B_0^x are tunable constant parameters. $x \equiv \frac{\mathbf{r}}{\frac{R}{1+\alpha\psi}}$ where α is the solute expansion coefficient.

3.5 Equation of Motion

The free energy functional of a closed system can fully describe the static thermodynamic state of a system in equilibrium. However, for a system out of equilibrium, additional equations must be satisfied to determine how the system will evolve in time. These equations of motion are chosen to drive the system towards equilibrium by minimizing the free energy functional, as required by thermodynamics.

Atomistic models like Monte-Carlo allow the system to evolve in time through the discrete movement of individual atoms. Continuum models are coarse-grained to neglect these degrees of freedom, and thus must be advanced through general thermodynamic principles. Further constraints on the system can be introduced through conservation laws that limit how the continuum field(s) can progress in time.

3.5.1 Model A: Nonconserved Dynamics

Nonconserved dynamics advance the free-energy functional of a system towards equilibrium without the restriction of a conservation law:

$$\frac{\delta\phi}{\delta t} = -(M\frac{\delta F}{\delta\phi}) \tag{3.21}$$

where ϕ is a field which tracks a given property or feature of the system and is typically referred to as an order parameter. In addition, t is time, F is the free energy functional chosen for the system under examination, and M is a mobility coefficient. Noise has been neglected in this equation, but a stochastic noise term can be added on the right-hand side to model fluctuations.

The above equation describes the rate of change of the field ϕ with time. As the free energy works towards a minimum it is not restricted to a constant local ϕ. Furthermore $\frac{\delta\phi}{\delta t}$ does not need to bring the system into local equilibrium during the evolution, instead allowing it to adopt unphysical results out of equilibrium.

The Swift-Hohenberg model was developed using nonconserved dynamics.

3.5.2 Model B: Conserved and Diffusive Dynamics

In simulations using conserved dynamics, the free-energy functional is minimized under the constraint that the total flux of some quantity in the system is conserved. The flux used as a constraint could be any conserved field, like mass, momentum, thermal energy, etc.

$$\frac{\delta n}{\delta t} = \nabla(M\nabla\frac{\delta F_{PFC}}{\delta n}) \tag{3.22}$$

By solving equation 3.22, the system can only progress in a fashion that lowers free energy while also holding constant the local amount of n. Constraining the system to hold constant the local density means that mass must travel through the system by physically diffusing across a distance. The simple description of PFC described in section 3.1 is evolved through conserved dynamics as are most descriptions of PFC. Noise can also be added to the right-hand side of the above equation.

Chapter 4

METHODS

To understand the underlying physics behind the formation and growth of a liquid film, the structural disjoining potential was introduced in section 2.4. As stated previously, an exponential form has been proposed to describe the short-ranged structural interactions that cause repulsive behaviour:

$$V_{rep}(h) = 2\gamma_{SL} + \Delta\gamma \exp(\frac{-h}{\delta}) \tag{4.1}$$

Where $\Delta\gamma = \gamma_{GB} - 2\gamma_{SL}$ and δ is an interaction length on the order of the atomic spacing. Similarly, a form has been proposed for a disjoining potential with an attractive minimum,

$$V_{att}(h) = 2\gamma_{SL} + \Delta\gamma_1 \exp(\frac{-h}{\delta_1}) + \Delta\gamma_2 \exp(\frac{-h}{\delta_2}) \tag{4.2}$$

Equations 4.1 and 4.2 are helpful phenomenological forms to compare with simulated PFC results. However, without direct derivation from the underpinning thermodynamic theory these two equations serves only as a guide [11]. The disjoining potential can also be expressed as the competition between bulk and interfacial energies:

$$\gamma_{GB} = \Delta f_{bulk} h + 2\gamma_{SL} + V(h) \tag{4.3}$$

Taking the first derivative of this equation with respect to h yields a simple form:

$$\frac{\delta V(h)}{\delta h} = -\Delta f_{bulk} = V'(\mu) \tag{4.4}$$

This is known as the disjoining pressure, and is only a function of the chemical potential. By plotting disjoining pressure against width and integrating, $V(h)$ can easily be recovered. The advantage of this method is that far fewer quantities need to be calculated, namely f_{liquid}, f_{solid} and h. In addition, in order to integrate analytically, $V'(\mu)$ will be fit to an exponential form like equation 4.1 or equation 4.2.

The calculation of $V(h)$ will be discussed in the following sections. First, the detailed parameter choice and model specifics will be presented.

4.1 Grand Canonical Ensemble

As the system approaches the melting point, the grain boundary region becomes increasingly disordered, until forming a liquid-like film and eventually completely melting. Instead of using temperature as the intensive variable to control this phenomenon and vary $V(h)$, chemical potential can be chosen instead. In this analogous scheme the system becomes more disordered as μ approaches the solidus line (μ_{EQ}), and can be described using the grand canonical ensemble instead of the Gibbs ensemble. This scheme was also chosen by Mellenthin et al. [18], whose work will be directly compared with the results presented in section 5. Since the system contains both concentration and density fields, the grand potential can be calculated as follows:

$$\omega = F_{PFC} - \mu_\psi \psi - \mu_n n \tag{4.5}$$

where F is the PFC free energy,

$$F_{PFC} = \int (\frac{n}{2}(\Delta B_0 + B_2^l \psi^2 + B_0^x (1+\nabla^2)^2)n - \frac{t}{3}n^3 + \frac{v}{4}n^4 + \frac{w}{2}\psi^2 + \frac{u}{4}\psi^4 + \frac{K}{2}|\Delta\psi|^2)dx \tag{4.6}$$

μ_ψ is the chemical potential of concentration, μ_n is the chemical potential of density, n is the dimensionless number density and ψ is the dimensionless concentration field. The chemical potential of concentration and the chemical potential of density can be stated as follows:

$$\frac{\delta F_{PFC}}{\delta \psi} = \mu_\psi = (w + n^2 B_2^l - K\Delta^2)\psi + u\psi^3 \tag{4.7}$$

$$\frac{\delta F_{PFC}}{\delta n} = \mu_n = (\Delta B_0 + B_2^l \psi^2 + B_0^x (1 + \nabla^2)^2) n - tn^2 + vn^3 \tag{4.8}$$

Chemical potential of concentration that was chosen to be varied intensive quantity, while the chemical potential of density and temperature were held constant. The values for constants mentioned here are specified in section 4.3.2

4.2 Equations of Motion (EOM)

Model B is the usual choice for PFC simulations. It has built-in mass conservation, and thus can give physical results while the system evolves. However, this means the system must advance at diffusion-limited speeds. Premelting is an equilibrium phenomenon, which means that accurate dynamics are not a concern for its study. Model A dynamics do not have this diffusion-limited behavior and drive the system more quickly towards an equilibrium state, as was done by Mellenthin et al. [18] A lagrange multiplier is introduced to equation 4.9 and 4.10 to force the chemical potentials of the system to evolve to the values of the langrange multiplier. For a binary alloy two equations of motion must be satisfied:

$$\frac{\delta n}{\delta t} = -(M \frac{\delta F}{\delta n}) - \mu_n \tag{4.9}$$

$$\frac{\delta \psi}{\delta t} = -(M \frac{\delta F}{\delta \psi}) - \mu_\psi \tag{4.10}$$

Where the lagrange multiplier is written as the chemical potential of the density or concentration field, i.e. μ_n or μ_{psi}, respectively. Since the system picks values for concentration and density based on the chosen chemical potential and energy minimization, the dynamics of the concentration and density fields are nonconserved for this study. Finally it should be noted that the nonconserved model A dynamics cannot simulate phase coexistence as model B dynamics do, in which there is coexistence for a range of simulation parameters (in this case the system average density) at a given temperature. Instead, there will only be coexistence between the solid and liquid phases at a single chemical potential, the melting point, for a given temperature.

4.3 System Characteristics

A search of parameter space in μ_ψ was conducted until a premelting region was discovered. Chemical potential for our system is negative and increases (gets more positive) as it approaches the solidus. Since chemical potential is normalized, it can be either positive or negative.

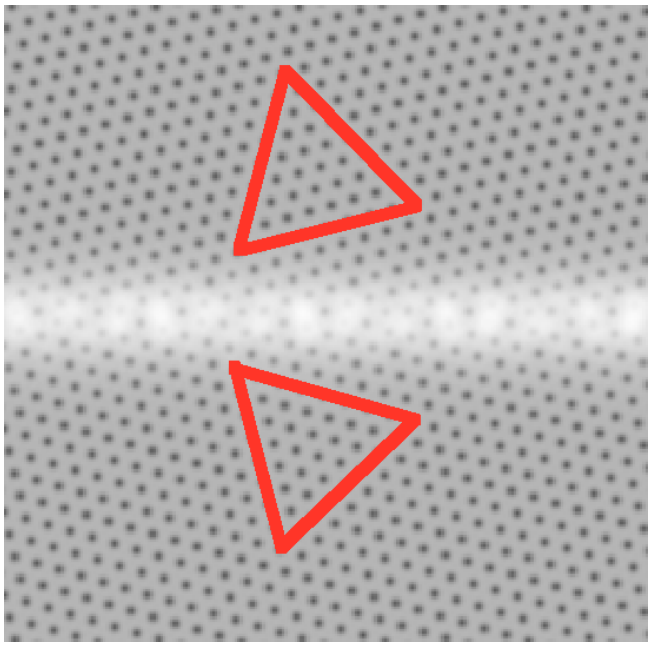

Figure 4.1: Highlighted lattice points in the concentration field show the differently oriented crystal grains forming a grain boundary. The system is far into the solid region ($\mu_\psi = -0.029951$) at a misorientation of $\theta = 27.8^o$.

A triangular crystal structure (see figure 4.1) was chosen to model grain boundaries (in 2D) because of its simplistic construction as periodic solutions of the PFC free energy functional. The system 'window' is a square box of size N_xxN_y, where N_x and N_y are the lengths (in grid points) of the system in the x and y-directions, respectively. Even though the system was simulated with periodic boundary conditions, in both the x and y directions, there are issues with fitting a triangle lattice in a square box. Since an integer number of density peaks cannot fit in both directions, some number of lattice sites will feel some amount of strain as they compress into the box. While PFC can easily manage this elastic effect, however this accommodation will alter the free energy density of the solid.

This problem can be partially mitigated by choosing specific misorientations that allow the lattice to more easily 'fit' into the size restraints. The size of the numerical grid spacing (δ_x or δ_y) can also be tuned independently to lower the contribution of strain to free energy density. In the model presently being used, however, $\delta_x = \delta_y$ is fixed, so a small additional strain component to the free energy density is expected in our simulations. Numerical grid spacing is in dimensionless spacial units of the free energy functional. In addition, it should be noted that due to the periodic boundary conditions, two grain boundaries exist in the simulation - one in the centre, and one split between the top and bottom of the image, as seen in figure 4.2.

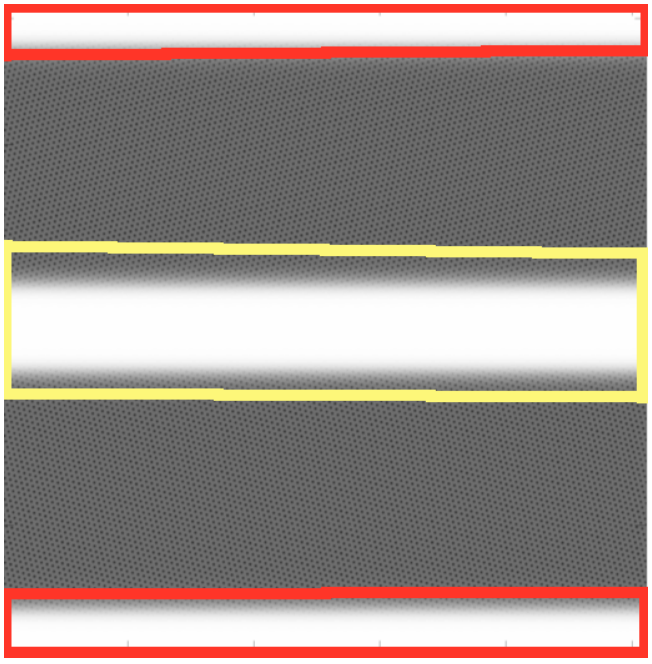

Figure 4.2: Highlighted regions in the concentration field show the two different grain boundaries one in red, and one in yellow. The system is significantly premelted ($\mu_\psi = -0.0249686$) at a misorientation of $\theta = 27.8^o$

4.3.1 Simulations

To simulate a grain boundary the initial condition of the system is set as two crystal grains set a distance apart with liquid between them. Each grain is rotated by $\frac{\theta}{2}$, as seen in Figure 4.1. The solid phase is seeded by setting the density field to a triangular crystal described

in terms of sinusoids. The density in the liquid region is specified by being set to an initial constant value. A μ_ψ is chosen for the system, and held constant as the simulation is evolved in time. Equilibrium is reached when the system has ceased to change - i.e. when the local measured μ_ψ is equal to the total μ_ψ imposed on the system from the initial conditions. It is at this point that measurements of the system's energy are taken.

4.3.2 System Values

	w	0.088
	u	4.0
	t	0.6
	v	1.0
	B_l^2	-1.8
Values for PFC simulations:	Grid spacing $\delta_x = \delta_y$	$\frac{\pi}{4}$
	B_x	1.0
	Dimensionless scaled temperature $dB0$	0.05
	μ_n	1.05
	System size	1024x1024

4.4 Width Calculation

Measuring the film width is an essential step to calculating the disjoining potential. From the film width, important information about the interface interactions can be inferred. However, what constitutes the width of a premelted grain boundary is not well defined in the literature. Indeed, the nanometer scale film is so small that for most premelted boundaries, the overlapping interfaces keep the film from truly reaching the bulk liquid. Only the largest widths, nearest to the solidus, have values close to bulk liquid properties. These large widths have a near-zero disjoining potential, which makes them uninteresting for the current discussion.

While a variety of width finding techniques have been applied in the literature, the chosen technique for this study was an excess mass calculation detailed in Mellenthin et al. (2008) [18]. This calculation technique takes advantage of the additional disorder that occurs as the grain boundary approaches the solidus, and its deviation from bulk values. Excess mass can find a width value from the amount of deviation even when a film is not evident. Not only does this technique allow low width films to be probed, but it also

collects data on completely dry grain boundaries providing a baseline for comparison. The subsequent discussion will not differentiate between boundaries where a film is visually present and where it is not.

It is helpful to consider a reference system made only of bulk liquid and bulk solid. Comparing a grain boundary system to these bulk components, a region of bulk solid can also be identified for some portion of the crystal grains. The remaining liquid-like region will have some measure of similarity to a bulk liquid, depending on how close to the solidus the system is. With this idea, a ratio can be expressed as the variation of the grain boundary system from the reference system.

$$n_{excess}(\mathbf{r}) = \frac{n(\mathbf{r}) - n_S}{n_L - n_S} \tag{4.11}$$

Where $n(r)$ is the dimensionless number density field, n_S is the average density in the bulk solid and n_L is the average density in the bulk liquid. Equation 4.11 approaches zero when the grain boundary is dry, and approaches 1 when the film is large, it will however never reach either of these values since some difference will remain due to an interface present in the system. For a binary alloy, either the concentration or density field can be chosen for this calculation. For this study, density was chosen in order for a more direct comparison with pure material results, which can only use a density field.

$$h = \frac{\sum n_{excess}(r)\delta_y L_y}{N_x L_y} \tag{4.12}$$

4.5 Finding the Structural Disjoining Potential

Solving for the disjoining potential from the disjoining pressure, $\frac{\delta V(h)}{\delta h}$, is a straightforward exercise. The only values necessary are from the bulk grand potential energies, and the grain boundary width. Twelve values for chemical potential were selected as snapshots of the system at different stages in the premelting process. For each chemical potential chosen, three systems were run: a completely solid system, a completely liquid system, and a grain boundary system. The bulk solid system was initialized in a similar manner to the grain boundary system; however there was no angle of misorientation and only a solid region was seeded. The bulk liquid system was seeded with only liquid phase. Five angles of misorientation were chosen based on the low-strain calculations done by Mellenthin et al: 27.8^o, 21.8^o, 17.8^o, 13.2^o, 5^o. [18]The misorientation angles are a mix of high, low

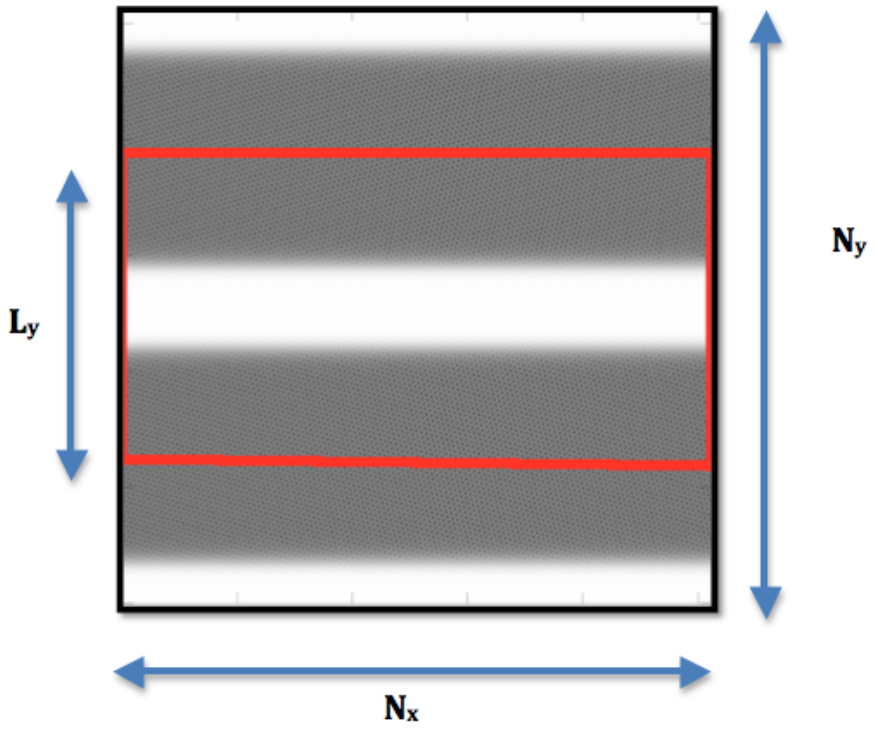

Figure 4.3: The window method allows a region (red) to be specified that corresponds to only one grain boundary.

and intermediate angle boundaries. $V(\mu) = \omega_{solid} - \omega_{liquid}$ will be the same for all angles, and thus the only quantity that changes throughout these angles is width. To recover the disjoining potential the curve of disjoining pressure with respect to width was fit to an exponential function similar in form to equation 4.2. While this assumes the form of the disjoining potential to be exponential, there is good agreement in the literature with this form [11][2] and this study is no different. While the grain boundary for 27.8^o had enough points to plot values for low and high widths, the other angles only had data for lower values. In order to accurately fit the other misorientations it was necessary to include higher width points. Since all misorientations should go to the same value of disjoining pressure at high widths, points were selected from the limit shown by 27.8^o and inserted into the plots of the other misorientations at very high widths. It was also observed that 27.8^o was going to a non-zero value of disjoining pressure for high widths. For reasons discussed in the next chapter, a non-zero high width limit is undesirable, thus once all angles had

been fit to a curve a constant value equal to the high width limit was subtracted from them. The fit equation for the disjoining pressure, which now went to zero for large widths, was then analytically integrated to produce an equation for the disjoining potential.

Chapter 5

RESULTS AND DISCUSSION

5.1 Results

Varying misorientation is a very useful method of investigating the structural disjoining potential. In this section results are presented for the angles of 27.8^o, 21.8^o, 17.8^o, 13.2^o and 5^o. This range neatly maps out the behaviour of the premelted film width and associated disjoining potential with the transition from high-angle to low-angle grain boundaries.

Figure 5.1 shows the nature of the increase in premelted film width with chemical potential. Since width was calculated using the excess mass technique, a dry grain boundary (i.e. a boundary far into the bulk solid) will always have some finite width. Since excess mass is a measure of how far the grain boundary is from the properties of the bulk solid phase, low-angle boundaries will have a smaller dry grain boundary width than a high-angle boundary. Grain boundaries vary very little in width for the majority of the approach to the solidus (i.e. melting point). Only the 27.8^o high-angle boundary changes width rapidly as it diverges to infinity - representing a fully melted system. The 5^o low-angle boundary maintains a width close to its dry grain boundary width on its approach to the solidus. Past the solidus the 5^o boundary overheats, that is, continues to maintain solid phase in a region where the free energy favours the liquid phase. The grain boundaries at 21.8^o, 17.8^o, and 13.2^o lie somewhere between these two extremes. A melting point can be inferred from figure 5.1 where the grey dashed line is drawn. It is at this point that the boundaries for the angles $> 15^o$ melt completely, in line with what is expected for high-angle boundaries. The estimated chemical potential for the melting point is $\mu_{melt} \approx -0.025$.

The disjoining potential for 27.8^o displays a monotonically decreasing form in line with equation 4.1. As misorientation angle decreases, an attractive minimum forms and gets

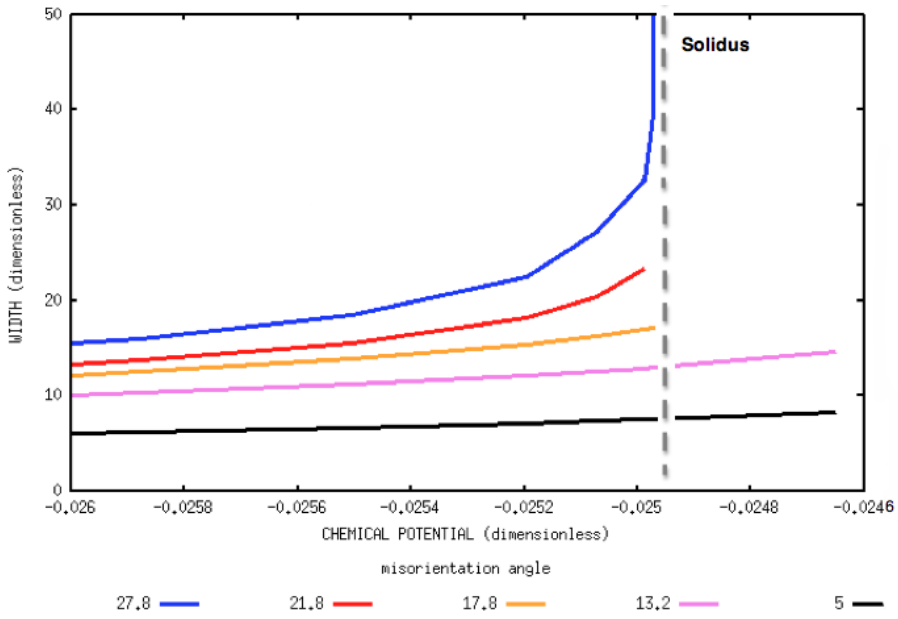

Figure 5.1: The width of a premelted grain boundary vs. chemical potential of concentration. The grey dashed line is the solidus line as predicted by where the grain boundaries completely melt. The width was determined using an excess mass calculation and is in terms of the lattice spacing.

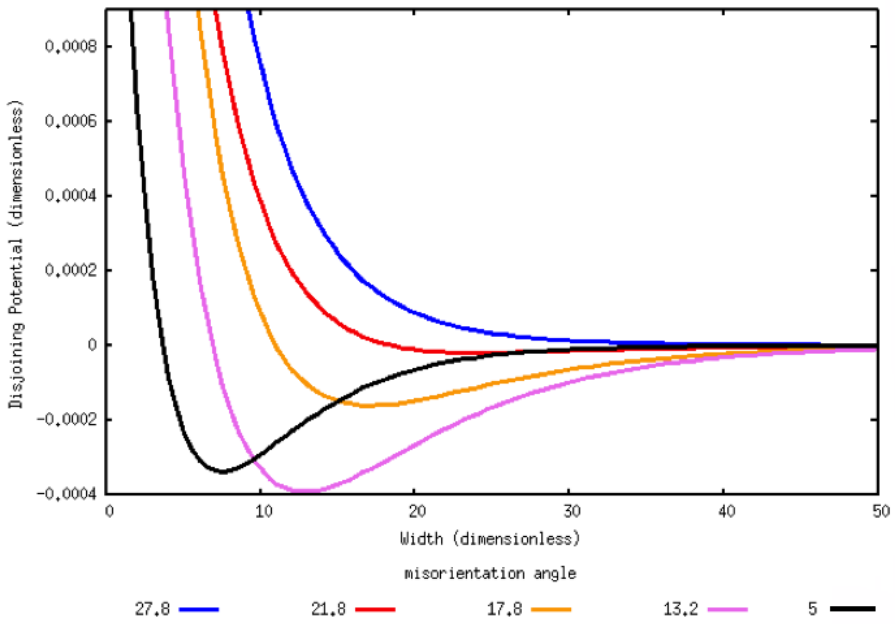

Figure 5.2: Disjoining potential vs. width as determined from $\int V'(\mu)$. The disjoining potential goes to zero in the limit of large widths for all misorientations.

deeper, which is better described by equation 4.2. The appearance of an attractive minimum marks the change between repulsive and attractive-repulsive behaviours. With an increase in misorientation the width predicted by the attractive minimum increases. The attractive minimum holds the grain boundary width around this minimum value as the system approaches the solidus, and for the lowest angle cases, past the solidus as well. Mishin et al. [19], also found that as the depth of the well increased with decreasing misorientation, which holds here except for 5^o. Likely, not enough points were gathered for 5^o for the fit to capture this behaviour. A more detailed study of these attractive-minimums could correct the depth of the 5^o minimum. The y-intercept for the disjoining potential corresponds with the grain boundary energy for a completely dry grain boundary. [18] Therefore it is expected as misorientation decreases, grain boundary energy decreases, which is the case in figure 5.4.

5.2 Discussion

Plotting the disjoining pressure vs. width reveals a negative exponential form that can be expected from the first derivative of equation 4.1. However, after fitting all angles of grain boundaries to an exponential curve, it is observed that they have a disjoining pressure that does not go to zero in the limit of large widths. A non-zero high-width disjoining pressure would mean that the disjoining potential would also never go to zero at large widths for these boundaries. Disjoining potential must go to zero at high widths because otherwise it effectively means that no matter what the size of the liquid-like film the two solid-liquid interfaces would always be able to interact, which is not a physical result. A physical result can still be determined from these two grain boundaries by shifting the curves up by a constant amount until they reach zero, as seen in figure 5.3. This non-zero value for large widths is likely due to strain effects, which can also be seen through the shift in the melting point.

The grain boundary width vs. chemical potential predicts a chemical potential of $\mu_{melt}^{GB} \approx -0.025$ as the melting point. A plot of the grand potential of the bulk liquid and solid vs. chemical potential predicts a value of $\mu_{melt}^{Bulk} \approx -0.024$. The melting point as predicted by the grain boundary systems, μ_{melt}^{GB}, agrees across all misorientations. This suggests that the cause of the discrepancy affects all systems equally. A strain imposed on the system due to the misfit of the triangular lattice in the simulation window would cause a shift in the grand potential. The system would melt at a smaller chemical potential due to an increase in free energy density in the solid lattice for all misorientations. If the misorientations chosen all impose zero, or a constant low strain on the system, then

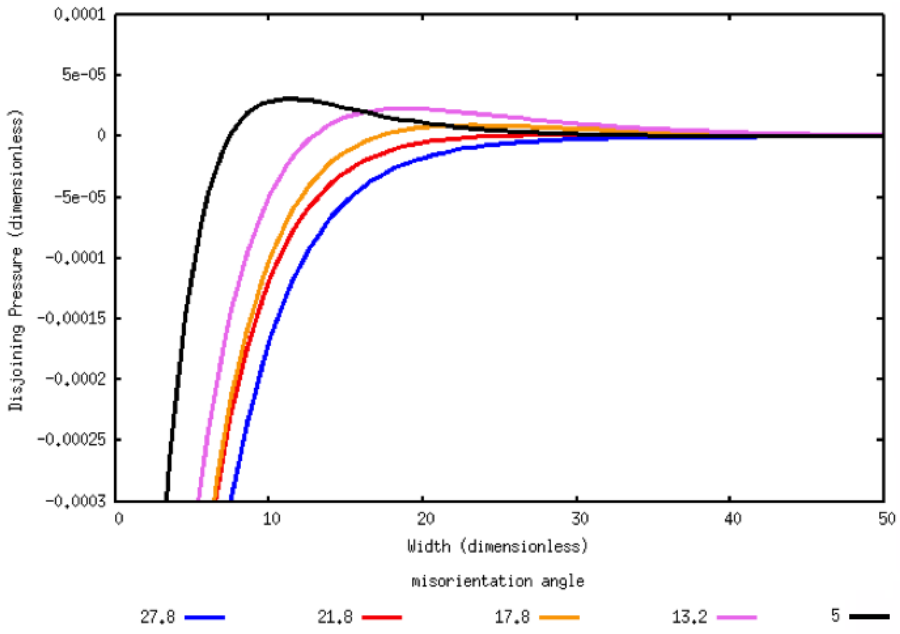

Figure 5.3: Disjoining pressure vs. width as determined from $V'(\mu) = \gamma_S - \gamma_L$ plus a shifting term. The disjoining pressure now goes to zero in the limit of large widths for all misorientations.

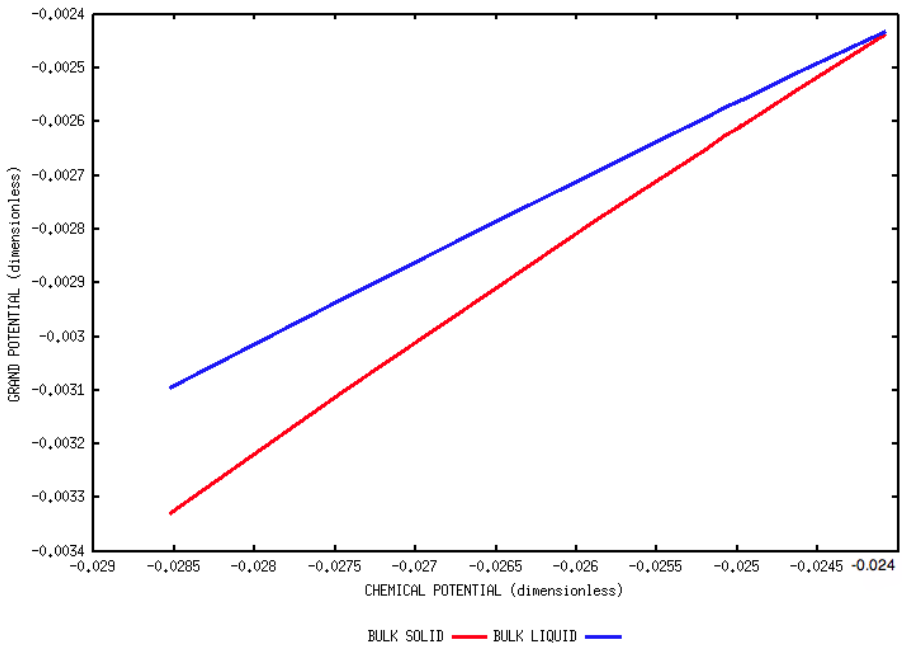

Figure 5.4: The grand potential calculated for the bulk solid and bulk liquid. Data was acquired from simulations of completely liquid and completely solid systems. A melting point is predicted at the intersection of these two lines, which gives: $\mu_{melt}^{Bulk} \approx -0.0240813$

a strain is likely caused by the grid spacing as discussed in section 4.3. A similar effect would also apply to the bulk solid simulation. For this system the misorientation is zero which means that the triangular lattice will be arranged so that the bases of the triangles will be arranged parallel to the x-direction. A brief analysis can be done to determine if an integer number of density peaks can fit in the system in the x and y-directions. If it can then the system should not be strained.

The grid spacing for the x-direction is defined as $\delta_x = \frac{\pi}{4}$. The number of peaks, P in the x-direction is given by:

$$P_x = \frac{N_x \delta_x}{\alpha} \tag{5.1}$$

where $N_x = 1024$ is the system size in the x-direction, and $\alpha = 2\pi$ is the lattice parameter. This results in a total of 128 peaks in the x-direction. For the y-direction, a rectangle shape can be used to count the number of peaks which is constructed from two triangles arranged tip-to-tip. The number of peaks in the y-direction can be given by:

Figure 5.5: Alignment of the triangular lattice for zero misorientation.

$$P_y = \frac{N_y \delta_y}{\alpha\sqrt{3}} \tag{5.2}$$

Where for the simulations presented here $\delta_x = \delta_y$, and the result is $P_y \approx 73.9$. This value represents the number of peaks the system would have with zero strain. The system will still have an integer number of peaks in the y-direction, but with a slight strain. Although this may seem like a small amount, because the disjoining potential is sensitive to small changes in energy, this could potentially have a large impact.

The effect of strain on the bulk solid system is to shift the ω_{solid} curve up, causing the melting point prediction for the bulk system to be an underestimate. This shift in bulk solid system energy also impacts the calculation of the disjoining pressure. The strain likely does not affect the grain boundary system and the solid system to the same degree. Since the shift introduces more energy, when investigating a value for a given potential, the value actually measured effectively corresponds to a chemical potential further along the same curve. Therefore it is likely that the values for $\omega_S - \omega_L$ and h that are supposed to be at the same chemical potentials likely relate to different chemical potentials. This is a potential reason for the shift seen in disjoining pressure for all angles. However, since the strain value shifts the system by a constant value, some of the strain can be accounted for in the analysis and removed.

A visual inspection of the 2D concentration field reveals the necessity for an excess mass formulation of the film width. Figure 5.6 illustrates grain boundaries for two of the five chosen angles of misorientation at chemical potentials close to the solidus. Only

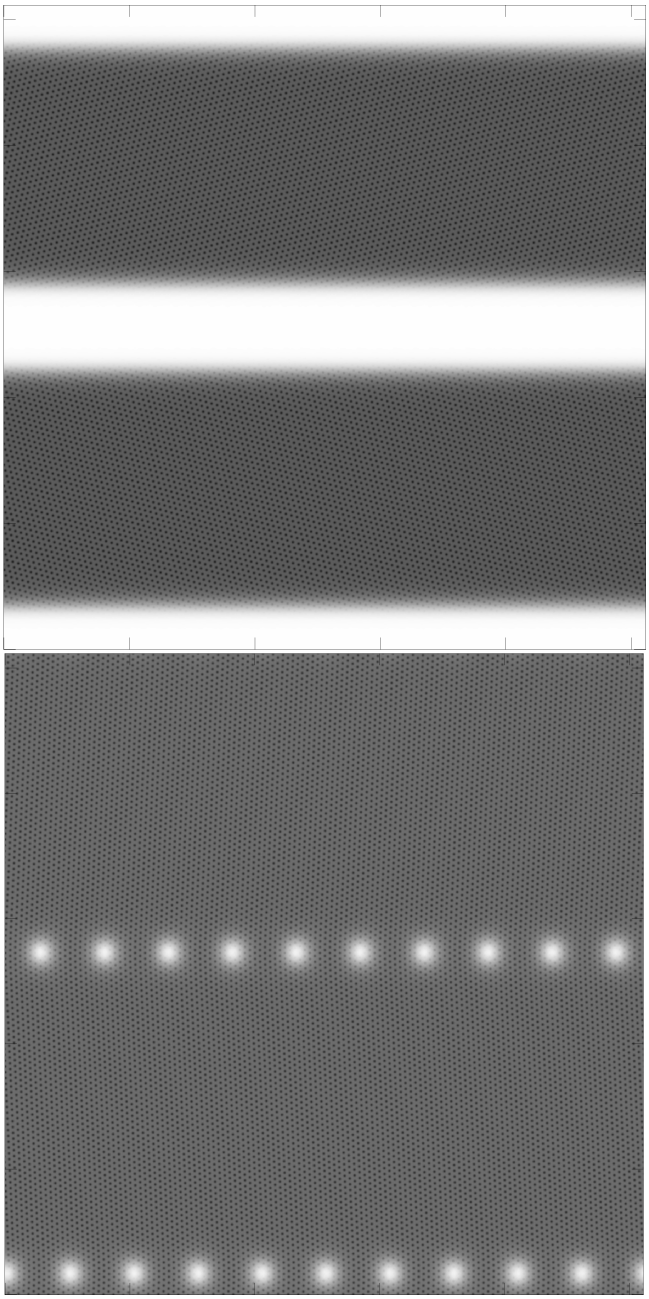

Figure 5.6: 2D concentration fields of grain boundaries at different misorientations close to the melting point. Dark regions are solid, light regions are disordered or liquid-like. Left: 5^o at $\mu_\psi = -0.0246499$, Right: 27.8^o at $\mu_\psi = -0.0249686$

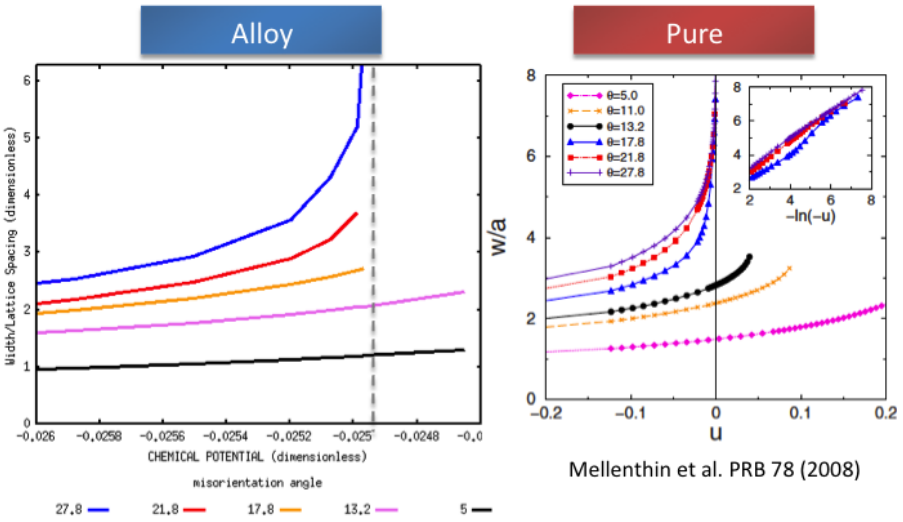

Figure 5.7: Comparison of results from this study to the pure material results of Mellenthin et al. [18], For Mellenthin et al., axis are in terms of u, which is a scaled chemical potential, and width over lattice spacing. Both are simulated using PFC

one out of five grain boundaries exhibits a noticeable liquid-like film. Three of the grain boundaries are technically high-angle ($> 15^o$), and thus it might be expected that they would all demonstrate visible liquid films. However, the range of chemical potentials will show visible signs of premelting is very narrow. Mellenthin et al showed similar results in their study of pure material grain boundary melting using PFC, as seen in figure 5.7. Although the scales between the two plots are not the same, it appears that angles 21.8^o and 17.8^o progress further towards the solidus than the pure material before they show a divergence in width.

It becomes more difficult to compare the pure material (figure 5.8) and alloy (figure 5.2) for the disjoining potential. In a multi-phase field study by Mishin et al., the pure material and alloy were compared [19]. It was found that the minimum width specified by a given grain boundary configuration didn't greatly change between alloy and pure material, however the depths of the minimum were increased in the alloy over the pure material. Since for the present study $2\gamma_{SL}$ is not known, a direct comparison of the depth of the minimum with the Mellenthin et al. pure results can not be done at this time. However it can be seen that as the misorientation decreases, the alloy produces an attractive minimum before the pure material. Also the shape of the 'well' produced by the minima is far less broad in the alloy than the pure material, suggesting it is in fact deeper.

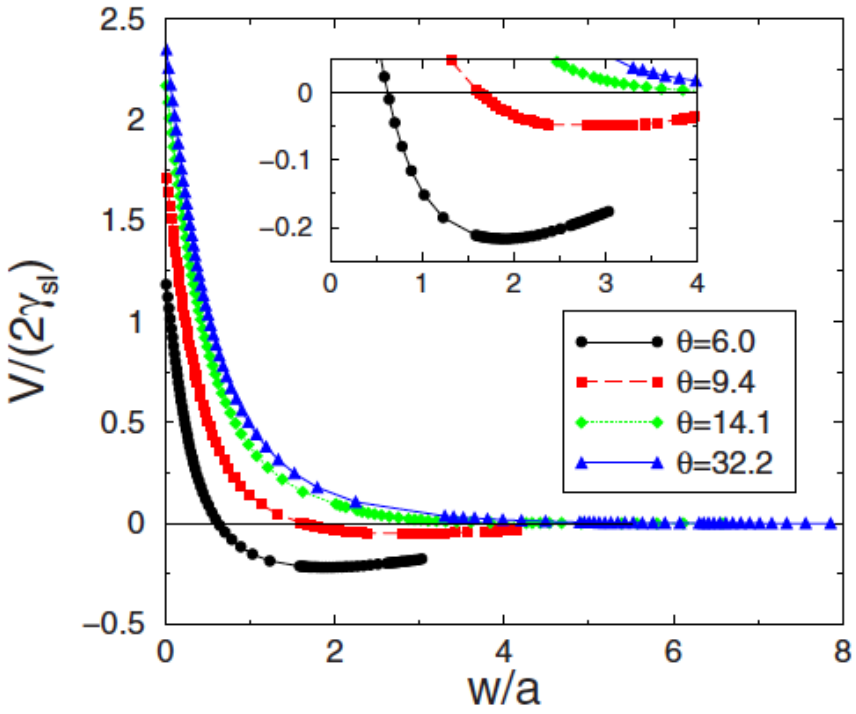

Figure 5.8: Disjoining potential vs. width from [18] for a pure material. Simulated using PFC

5.3 Conclusion

Despite residual strain effects from fitting the crystal lattice into a square system, phenomenological forms for the disjoining potential were produced that are in line with previous work. The disjoining potential was found to have an exponential form that was large at small widths and went to the limit of zero at large widths. Misorientation angle determined the size and shape of the disjoining potential curve, including influencing the y-intercept which is equal to γ_{GB}. Comparing to the pure material from Mellenthin et al. [18], the alloy was found to have much more pronounced attractive minimum in the disjoining potential, and it reached larger premelted widths faster for repulsive grain boundaries.

References

[1] A.M. Alsayed, M.F. Islam, J. Zhang, P.J. Collings, and A.G. Yodh. Premelting at defects within bulk colloidal crystals. *Science*, 309(78):184110, November 2005.

[2] J. Berry. Liquid-solid systems out of equilibrium: Phase-field crystal studies of solidification, melting, and plasticity. *McGill University (Ph.D Thesis)*, October 2011.

[3] G. Besold and O.G. Mouritsen. Grain-boundary melting: A monte carlo study. *Physical Review B*, 50(10):6573–6576, 1994.

[4] G. Besold and O.G. Mouritsen. Competition between domain growth and interfacial melting. *Computational Materials Science*, 18(2):225Äì244, 2000.

[5] D.R. Clarke. On the equilibrium thickness of intergranular glass phases in ceramic materials. *The Journal of American Ceramics*, 70:15–22, 1987.

[6] K. R. Elder and Martin Grant. Modeling elastic and plastic deformations in nonequilibrium processing using phase field crystals. *Physical Review E*, 70:051605, Nov 2004.

[7] K. R. Elder, Zhi-Feng Huang, and Nikolas Provatas. Amplitude expansion of the binary phase-field-crystal model. *Physical Review E*, 81(78):184110, November 2010.

[8] K. R. Elder, Nikolas Provatas, Joel Berry, Peter Stefanovic, and Martin Grant. Phase-field crystal modeling and classical density functional theory of freezing. *Physical Review B*, 75(78):184110, November 2007.

[9] K.R. Elder, M. Katakowski, M. Haataja, and M. Grant. Modeling elasticity in crystal growth. *Physical Review Letters*, 88:245701, Jun 2002.

[10] H. Emmerich, H. Lowen, R. Wittkowski, T. Gruhn, G.I. Toth, G. Tegze, and L. Granasy. Phase-field-crystal models for condensed matter dynamics on atomic

length and diffusive time scales: an overview. *Advances in Physics*, 61, December 2012.

[11] Saryu J. Fensin, David Olmsted, Dorel Buta, Mark Asta, Alain Karma, and J. J. Hoyt. Structural disjoining potential for grain-boundary premelting and grain coalescence from molecular-dynamics simulations. *Physical Review E*, 81(78):184110, November 2010.

[12] V. K. Gupta, D. H. Yoon, Meyer H. M. III, and J. Luo. Thin intergranular films and solid-state activated sintering in nickeldoped tungsten. *Acta Materialia*, 55, January 2007.

[13] J.J. Hoyt. Phase transformations. 2011.

[14] Ryoichi Kikuchi and John W. Cahn. Grain-boundary melting transition in a two-dimensional lattice-gas model. *Physical Review B*, 21:1893–1897, Mar 1980.

[15] R. Lipowski. Melting at grain boundaries and surfaces. *Physical Review Letters*, 57(22):2876, 1986.

[16] J. Luo. Stabilization of nanoscale quasi-liquid interfacial films in inorganic materials: A review and critical assessment. *Critical Reviews in Solid State and Materials Sciences*, 32:1–2, 67–109, 2007.

[17] J. Luo, V. K. Gupta, D. H. Yoon, and H. M. Meyer. Segregation induced grain boundary premelting in nickel-doped tungsten. *Applied Physics Letters 87*, 2005.

[18] Jesper Mellenthin, Alain Karma, and Mathis Plapp. Phase-field crystal study of grain-boundary premelting. *Physical Review B*, 78(78):184110, November 2008.

[19] Y. Mishin, W.J. Boettinger, J.A. Warren, and G.B. McFadden. Thermodynamics of grain boundary premelting in alloys: Phase-field modeling. *Acta Materialia*, 57(78):184110, November 2009.

[20] D. Olmsted, S.M. Foiles, and E.A. Holm. Survey of computed grain boundary properties in face-centered cubic metals: I. grain boundary energy. *Acta Materialia*, 57, August 2009.

[21] N. Provatas and K. Elder. *Introduction, in Phase-Field Methods in Materials Science and Engineering*. Wiley, 2010.

[22] T.V. Ramakrishnan and M. Yussouff. First-principles order-parameter theory of freezing. *Physical Review B*, 19:2775–2794, March 1979.

[23] M. Rappaz, A. Jacot, and W.J. Boettinger. Last-stage solidification of alloys: Theoretical model of dendrite-arm and grain coalescence. *Metallurgical and Materials Transactions A*, 34, March 2003.

[24] G.A. Somorjai and Y. Li. Introduction to surface chemistry and catalysis. June 2010.

[25] Victor M. Starov. *Wetting and Spreading Dynamics*. CRC Press.

[26] A.P Sutton and R.W. Balluffi. Interfaces in crystalline materials. December 2006.

[27] J.S. Wettlaufer and M. Grae Worster. Premelting dynamics. *The Annual Review of Fluid Mechanics*, 38, 2006.

[28] H. Wise and J. Oudar. Material concepts in surface reactivity and catalysis. January 2001.